

One Step Interface Activation of ZnS Using Cupric Ions for Mercury Recovery from Nonferrous Smelting Flue Gas

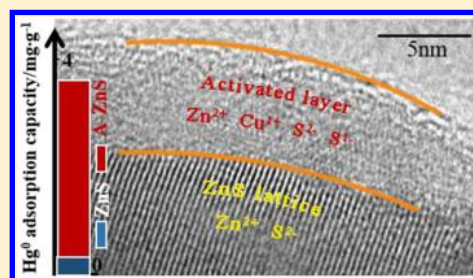
Yong Liao,[†] Haomiao Xu,[†] Wei Liu,[†] Hengfa Ni,[‡] Xiaoguo Zhang,[‡] Aiping Zhai,[‡] Zongwen Quan,[†] Zan Qu,^{*,†,‡} and Naiqiang Yan[†]

[†]School of Environmental Science and Engineering, Shanghai Jiao Tong University, Shanghai 200240, P. R. China

[‡]Henan Yuguang Gold & Lead Group Co. Ltd., Henan, Jiyuan 459000, P. R. China

Supporting Information

ABSTRACT: The flue gases with high concentration of mercury are often encountered in the nonferrous smelting industries and the treatment of mercury-containing wastes. To recover mercury from such flue gases, sorbents with enough large adsorption capacity are required to capture and enrich mercury. ZnS is a cheap and readily prepared material, and even can be obtained from its natural ores. In this work, a simple controllable oxidation method—soaking in cupric solution—was developed to improve the interfacial activity of ZnS and its natural ores for Hg⁰ adsorption. The gaseous Hg⁰ adsorption capacity of ZnS was enhanced from 0.3 to 3.6 mg·g⁻¹ after such treatment. Further analysis indicated that a new interface rich in S¹⁻ ions was formed and provided sufficient active sites for the chemical adsorption of Hg⁰. In addition, the cyclic Hg⁰ adsorption and recovery experiments demonstrated that the adsorption performance of spent activated-ZnS was recovered after reactivating sorbents with Cu²⁺, indicating the recovery of activated interface. Meanwhile, the high concentration of adsorbed mercury at the surface can be collected using a thermal treatment method. Utilization of raw materials from a zinc production process provides a promising and cost-effective method for removing and recovering mercury from nonferrous smelting flue gas.



1. INTRODUCTION

Mercury is a global pollutant and a great threat to human health owing to its toxicity, persistence, and bioaccumulation.¹ To scale down global mercury emissions, the Minamata Convention on Mercury has been put into force since 2017. As one of the main sources of anthropogenic mercury emission, mercury emitted from nonferrous metal smelters accounts for 20–40% of the emissions in China,^{2–4} which need to be strictly controlled to meet the requirements of the Minamata Convention.⁵ Similar to the coal-fired flue gases, there are also three states of mercury in smelting flue gas, namely, particle-bound mercury (Hg^p), oxidized mercury (Hg²⁺), and elemental mercury (Hg⁰), of which Hg⁰ usually accounts for 30–70% of the total mercury.^{6,7} Hg^p and Hg²⁺ can be effectively removed from flue gas using a combination of dust-cleaning apparatus and wet purification unit.^{8–10} However, owing to its volatility, insolubility, and chemical inertness, gaseous Hg⁰ is difficult to remove using common air pollution control devices.¹⁰ Therefore, the development of a specific technology is required to control gaseous Hg⁰ emission.

At present, the studies on mercury capture from flue gases are mainly concentrated on coal-fired flue gases, in which mercury concentration is ~1000 times lower than that in any nonferrous smelting flue gases. There still lack of any efficient methods to capture mercury from the flue gases with high concentration of it, especially for Hg⁰. The Boliden-Norzink technology, which employs HgCl₂ solution as the absorption reagent, has ever been used to capture Hg⁰ to produce

Hg₂Cl₂.^{11,12} However, the method appears to be less efficient and difficult to operate to meet the increasingly stringent emission demands. Also, the presence of SO₃²⁻, which is produced by simultaneous absorption of SO₂, can reduce Hg²⁺ in solution to gaseous Hg⁰, resulting in a high concentration of Hg⁰ in flue gas downstream of the absorption unit.^{13–15} To provide better removal and recovery of Hg⁰ from the gases, a viable alternative is to capture Hg⁰ by adsorption using a mercury-enrichment sorbent. The removal efficiency of Hg⁰ can easily be ensured by adjusting the amount of sorbent employed. Furthermore, the process is more promising if the sorbents can be readily prepared and recycled.

A variety of sorbents have been designed and tested for capturing gaseous Hg⁰ (e.g., carbonaceous sorbents, precious metal sorbents, transition metal oxides, and chalcogenides).^{8,16–19} However, most of these sorbents were investigated on the treatment of mercury from coal-fired flue gas, in which the concentrations of mercury and SO₂ are far lower than that in the nonferrous smelting flue gas. An optimal sorbent for removing gaseous Hg⁰ from smelting flue gas could be chalcogenides in view of their resistance to ultrahigh concentrations of SO₂ in smelting flue gas. In fact, it has been recognized that the mercury concentration in the concentrated ores (e.g., sphalerite in nature) used for zinc production is

Received: March 2, 2019

Accepted: March 11, 2019

Published: March 11, 2019

often far higher than in other ores, and that such ores appear to have a great natural affinity for mercury.^{11,20} This results in more mercury being emitted during zinc production. ZnS is the main constituent in raw zinc-concentrate ores, so ZnS is of interest as a sorbent for mercury enrichment.

Although ZnS has been investigated to capture gaseous trace-Hg⁰ from coal-fired flue gas,²¹ its Hg⁰ adsorption capacity and sorbent regenerative performance need to be enhanced to develop a cost-efficient sorbent for removing the ultrahigh concentrations of Hg⁰ that exist in smelting flue gas. The gas–solid contact interface is the primary space for mercury adsorption and sorbent regeneration; consequently, improving these performances by directly modifying the surface is of practical interest for both synthetic and natural ZnS. The developed polysulfide sorbents, such as FeS₂¹⁹ and [MoS₄]²⁻,²² exhibit better performance for the capture of gaseous Hg⁰ than ZnS does. It suggests that S_n²⁻ ions are more active than S²⁻ in the interfacial reaction of mercury adsorption. S_n²⁻ exists in a chain structure, in which S atom exists with a formal charge of S¹⁻ or S⁰.^{23,24} And S¹⁻ seems more conducive to the oxidation adsorption of Hg⁰ in terms of electron transfer. Transforming S²⁻ to S¹⁻ at the ZnS interface before adsorption appears to an effective way to improve the Hg⁰ adsorption capacity and regenerative performance of ZnS. But S²⁻ is easily oxidized to the stable but inactive S⁴⁺/S⁶⁺ (sulfite/sulfate) by oxidant, it is difficult to control the oxidation of S²⁻ to active S¹⁻. How to achieve the controllable oxidation of S²⁻? In the field of mineral flotation, cupric salts are generally used as activators to enhance the attachment of collector molecules to sphalerite surfaces.^{25,26} Weak oxidative Cu²⁺ ions can also oxidize the sphalerite surface, resulting in the production of S anions with higher valence than S²⁻.^{23,26} Therefore, Cu²⁺ ions may be a potential surface modifier for ZnS to improve its Hg⁰ capture performance.

In this study, aqueous Cu²⁺ was used to activate the interface of ZnS to develop a functional mercury-enrichment sorbent. The Hg⁰ adsorption performances of ZnS activated under different conditions were evaluated. The change in ZnS interface after activation and the mechanism responsible for improvement in Hg⁰ adsorption performance were also investigated. Furthermore, the regeneration of ZnS was studied to solve the decline in Hg⁰ adsorption activity after capturing Hg⁰.

2. EXPERIMENTAL SECTION

2.1. Sample Preparation. The natural zinc-concentrate ores employed as references (sphalerite, RZ) were provided by a zinc smelter, and pure ZnS samples were synthesized according to a hydrothermal method reported previously.²⁷ The details are given in the [Supporting Information \(SI\)](#).

2.2. Activation of the Zinc-Ore Concentrate and ZnS. Deionized water was used to dissolve metallic salt in this work. The concentrations of Ni(NO₃)₂, Fe(NO₃)₂, CuSO₄, CuCl₂, and CuBr₂ solution used were all 0.005 mol·L⁻¹, respectively. In addition, the concentrations of Cu(NO₃)₂ were varied from 0.001–0.01 mol·L⁻¹. ZnS or zinc-ore concentrate was just soaked in a Cu²⁺ solution without any other processes. The proportion used in the soaking was 1 mL liquid/mg of sorbent. After that, ZnS was successively washed using deionized water and ethanol, and then vacuum-dried at 60 °C for 9 h. Activated-ZnS was marked as A-ZnS, and samples soaked in 0.005 mol·L⁻¹ Cu²⁺ solution for 1, 5, 20, and 60 min were marked as A1-ZnS, A5-ZnS, A20-ZnS, and A60-ZnS,

respectively. Typically, the samples used in the cyclic adsorption experiments were activated in a fixed-bed quartz tube. A 0.005 mol·L⁻¹ Cu²⁺ solution was injected into the quartz tube to flow through the ZnS sorbent bed. The spent solution was recovered at the end of the quartz tube for the next activation. This process lasted for 1 min, and the activated sample was then washed and blown dry in a N₂ stream at 60 °C.

2.3. Experimental Methods. The fixed bed reactor system used to evaluate the Hg⁰ adsorption performance of sorbent was consistent with those used in our previous study.^{18,19,28} The device schematic of the evaluation system is shown in [SI Figure S1](#). The Hg⁰ adsorption experiment was performed in pure N₂ or in the simulated gases at 60 °C. The gas stream had a flow rate of 500 mL·min⁻¹ and contained 1.0–1.3 mg·m⁻³ of gaseous Hg⁰, which was supplied by a mercury permeator. For each Hg⁰ adsorption test, the concentration of Hg⁰ in the airflow was stabilized for 30 min before it was directed through the sorbent bed. The mass of sorbent used in the adsorption experiment was 20–50 mg.

During the cyclic Hg⁰ adsorption, Hg⁰ recovery, and sorbent regeneration tests, the sorbent underwent the following processes in turn: (I) first activation–1st adsorption–1st thermal treatment; (II) deionized water washing–2nd adsorption–2nd thermal treatment; (III) second activation–3rd adsorption–3rd thermal treatment; (IV) deionized water washing–4th adsorption–4th thermal treatment; and (V) third activation–5th adsorption–5th thermal treatment. The sorbent was not moved from the same quartz tube reactor to avoid mass loss during the above processes. The thermal treatment was conducted in a 700 mL·min⁻¹ N₂ stream, and the temperature rose from 50 to 450 °C at a heating rate of 5 °C·min⁻¹.

2.4. Characterization. The variations in the amounts of Cu and Zn ions in sorbent and liquid during activation were determined using an inductively coupled plasma spectrometer (ThermoScientific, ICAP6300). The BET surface areas, powder X-ray diffraction pattern (XRD) analysis, transmission electron microscopy (TEM) and high-resolution transmission electron microscopy (HRTEM), and X-ray photoelectron spectroscopy were conducted with a surface area and pore size analyzer (Quantachrome 2200e), an X-ray diffractometer using Cu K α radiation (Bruker-AXS D8 Advance), a JEM-2100F electron microscope, and an X-ray photoelectron spectrometer using Al K α radiation (ThermoFischer, ESCALAB 250Xi), respectively.

3. RESULTS AND DISCUSSION

3.1. Mercury-Enrichment Behavior of Various forms of ZnS Sorbents. Fresh ZnS exhibited the ability to capture gaseous Hg⁰. However, the Hg⁰ adsorption capacity of ZnS was only ~0.3 mg·g⁻¹ ([Figure 1a](#)), and the remove efficiency of ZnS for Hg⁰ was always lower than 10% during the test time (the corresponding Hg⁰ adsorption breakthrough curves were shown in [SI Figure S2](#)). They indicate that fresh ZnS was not competent for coping with flue gas containing high concentrations of Hg⁰. After soaking in deionized water, Ni(NO₃)₂, and Fe(NO₃)₃ solutions, no obvious change could be observed in their adsorption capacity and breakthrough curves, indicating that those substances had a negligible effect on Hg⁰ capture performance. Surprisingly, after soaking in Cu(NO₃)₂ solution, the Hg⁰ adsorption capacity of ZnS was greatly increased to ~3.6 mg·g⁻¹. Meanwhile, the removal

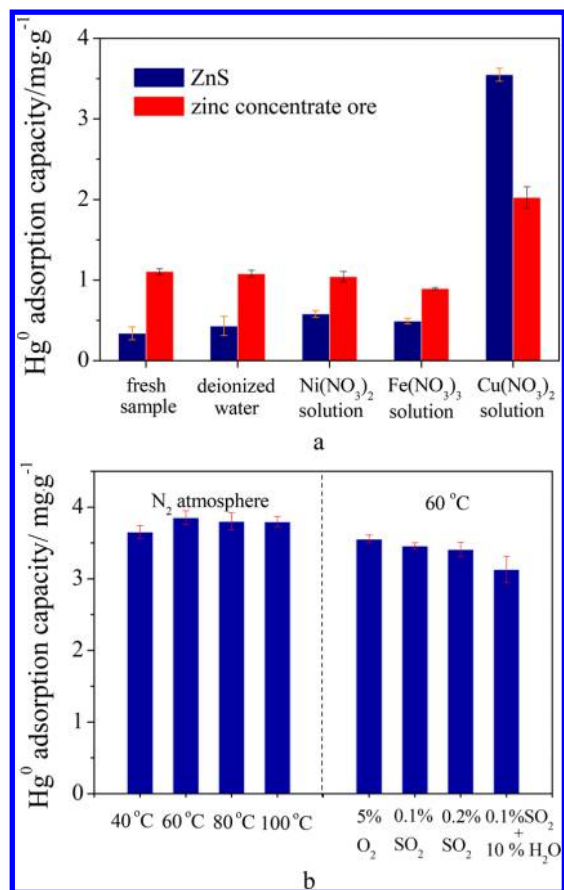


Figure 1. (a) Hg^0 adsorption capacities of ZnS and zinc-ore concentrate treated using different methods. (b) Hg^0 adsorption capacities of A5-ZnS at different atmospheres. Reaction conditions: sorbent mass = 20 mg, total flow rate = $500 \text{ mL}\cdot\text{min}^{-1}$, temperature = 60°C (for 1a), adsorption time = 3 h, $[\text{Hg}^0] = 1.1\text{--}1.2 \text{ mg}\cdot\text{m}^{-3}$.

efficiency was also significantly improved, with a total Hg^0 remove efficiency of 70%. These suggest that some interaction occurred at the interface between the ZnS phase and the $\text{Cu}(\text{NO}_3)_2$ solution, which improved the Hg^0 adsorption performance of ZnS.

The fresh zinc-ore exhibited better performance for Hg^0 capture than ZnS did, with a tested adsorption capacity of $\sim 1.1 \text{ mg}\cdot\text{g}^{-1}$ (Figure 1a). This might be because the complex associated metal sulfides in it such as pyrite (FeS_2), which shows better Hg^0 adsorption performance,¹⁹ contributed to Hg^0 capture. Likewise, only the adsorption performance of zinc-ore soaked in Cu solution was improved, and the adsorption capacity increased to $\sim 2.0 \text{ mg}\cdot\text{g}^{-1}$. The specific surface area of the zinc-ore was $0.4 \text{ m}^2\cdot\text{g}^{-1}$, which was much smaller than that of the synthesized ZnS ($19.3 \text{ m}^2\cdot\text{g}^{-1}$). The limited specific surface area may restrict improvement in the capacity after soaking in $\text{Cu}(\text{NO}_3)_2$ solution.

Figure 1(b) shows the Hg^0 adsorption capacities of A5-ZnS under different atmospheres. A5-ZnS showed excellent Hg^0 adsorption performance at $40\text{--}100^\circ\text{C}$ under N_2 atmosphere. The adsorption capacity of A5-ZnS slightly decrease after 5% O_2 was added into. This may be attribute to the minor oxidation of surface of A-ZnS by O_2 . When 0.1% SO_2 and 5% O_2 were added into the atmosphere, no obvious change in adsorption capacity was observed. And even if the SO_2 concentration further increased to 0.2%, the Hg^0 adsorption capacity of A5-ZnS was close to that in the absence of SO_2 ,

suggesting SO_2 have negligible effects on the Hg^0 adsorption performance of A-ZnS. Due to the competitive adsorption of H_2O and Hg^0 , the obvious inhibition of H_2O on Hg^0 adsorption have been widely reported.^{18,29,30} In the presence of 10% H_2O , the Hg^0 adsorption capacity of A5-ZnS only decreased slightly, indicating the good resistance to H_2O .

3.2. Surface Modification of ZnS by Various Cupric Solutions. The Hg^0 -capture performance of ZnS soaked in different cupric solutions was investigated to clarify the role of anions in this activation process. As shown in Figure 2a, the

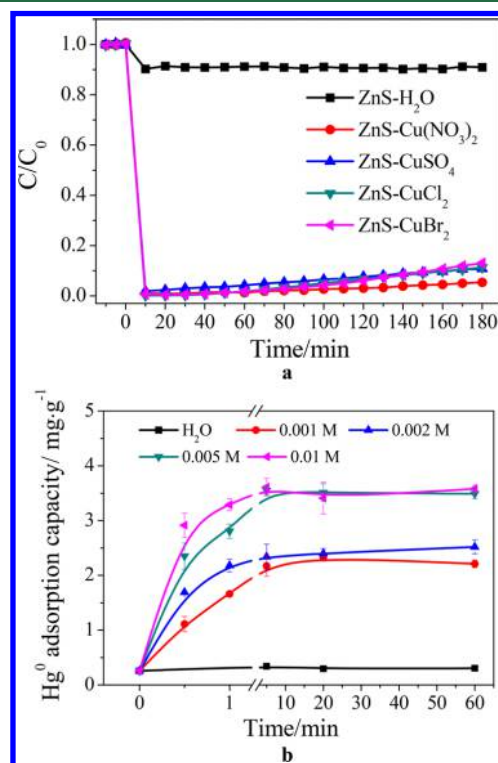


Figure 2. (a) Hg^0 adsorption breakthrough curves of ZnS soaked in different cupric solutions. (b) Hg^0 adsorption capacity of A-ZnS that was soaked in various concentrations of $\text{Cu}(\text{NO}_3)_2$ solution for various times. Reaction conditions: sorbent mass = 40 (for 2a) or 20 mg (for 2b), total flow rate = $500 \text{ mL}\cdot\text{min}^{-1}$, adsorption temperature = 60°C , adsorption time = 3 h, and $[\text{Hg}^0] = 1.0\text{--}1.1 \text{ mg}\cdot\text{m}^{-3}$.

Hg^0 capture performance of ZnS soaked in CuSO_4 solution was as good as that treated by $\text{Cu}(\text{NO}_3)_2$. Furthermore, there were also not obvious changes in adsorption performance when ZnS was treated by CuCl_2 and CuBr_2 solutions, even though halogens have good affinity for mercury.^{8,10} This implies that the contribution of anions to the improvement was negligible and that aqueous Cu^{2+} was the crucial factor that interacted with the ZnS surface to enhance the Hg^0 adsorption performance.

The effects of immersion time and concentration of aqueous Cu^{2+} on the Hg^0 adsorption performance of ZnS were also investigated (Figure 2b). The corresponding breakthrough curves (SI Figure S3) show that all A-ZnS sorbents absorbed as much gaseous Hg^0 as possible in the tests. When ZnS was soaked for 5 min, its mercury adsorption capacity increased from ~ 2.2 to $\sim 3.6 \text{ mg}\cdot\text{g}^{-1}$ with increase in the Cu^{2+} concentration from 0.001 to 0.005 $\text{mol}\cdot\text{L}^{-1}$. However, a sustained increase in capacity did not appear when the Cu^{2+} concentration was further increased to 0.01 $\text{mol}\cdot\text{L}^{-1}$. This

indicates the improvement of adsorption capacity was not only determined by the concentration of aqueous Cu^{2+} . In addition, the Hg^0 adsorption capacity of ZnS seemed to be optimal after 5 min activation, no matter what concentration of Cu^{2+} was in solution. Moreover, the Hg^0 adsorption capacity of ZnS exceeded 70% of its optimum after activation for 1 min. These results demonstrate that enhancement of the Hg^0 adsorption performance of ZnS by Cu^{2+} could be achieved rapidly.

3.3. Ion Exchange Between ZnS and Cupric Solution.

Figure 3 shows the variation in the amounts of Cu and Zn ions in the Cu^{2+}

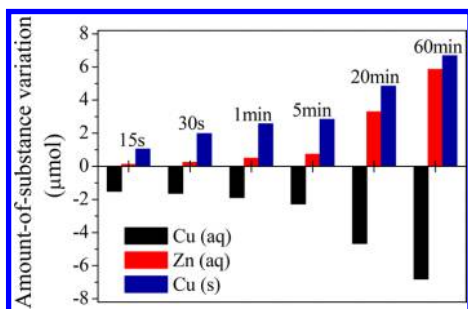


Figure 3. Variations in the amounts of Cu and Zn ions in the Cu^{2+} solution and the ZnS phase during activation.

in the solid and liquid phases during aqueous Cu^{2+} activation. An increase of Cu ions of $6.7 \mu\text{mol}$ was observed in the ZnS phase after soaking for 60 min, corresponding to a decrease of Cu ions of $6.8 \mu\text{mol}$ and an increase of Zn ions of $5.9 \mu\text{mol}$ in the Cu^{2+} solution. This suggests that Cu ions entered the lattice of ZnS and that some of the Zn ions were exchanged with Cu ions. This spontaneous ion exchange process has also been reported in other studies.^{31,32} Typically, only $<0.3 \mu\text{mol}$ of Zn ions were detected in solution, with a $2 \mu\text{mol}$ increase of the Cu ions in the ZnS phase, after soaking for 1 min. Moreover, the increase in Zn ions was always $1\text{--}2 \mu\text{mol}$ less than the decrease in aqueous Cu ions during activation. This hysteresis phenomenon indicates that $\sim 1\text{--}2 \mu\text{mol}$ of Cu ions were adsorbed to the surface of ZnS instantly, and that the adsorbed Cu then gradually diffused into the inner layer of ZnS, replacing the Zn ions in the lattice. Combining this with the results in Figure 1, we find that only $<3 \mu\text{mol}$ of Cu ions were required to enhance the Hg^0 -adsorption performance of 40 mg ZnS by a factor of 9 after 5 min activation.

3.4. Formation of the Activated Interface Layer.

The XRD patterns of ZnS (Figure 4a) before and after Cu^{2+} activation show that the diffraction peaks of all samples were consistent with the cubic sphalerite structure (JCPDS No. 05-0566). The diffraction peaks corresponding to other

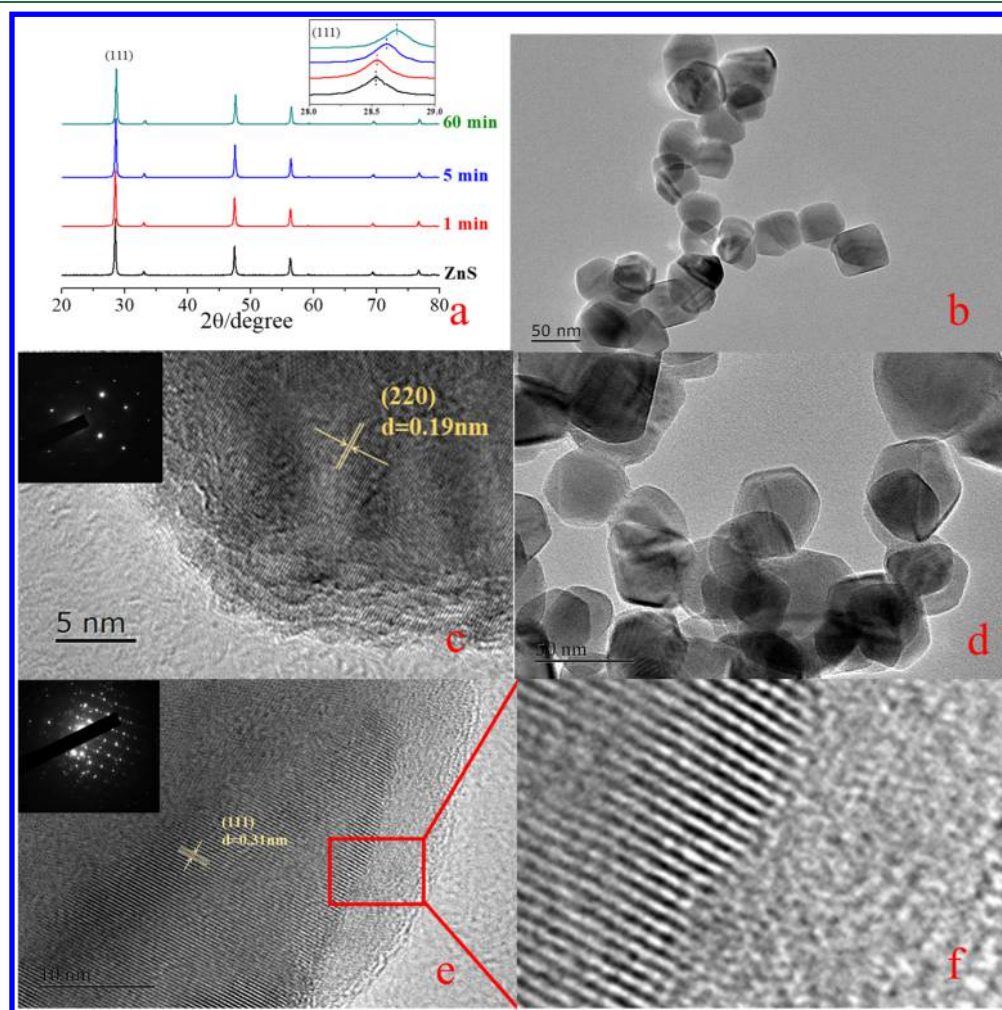


Figure 4. (a) XRD patterns of ZnS, A1-ZnS, A5-ZnS, and A60-ZnS. Inset: XRD patterns of (111) crystal facets. (b) TEM image of ZnS particles. (c) HRTEM image of a ZnS particle. Inset: The corresponding SAED pattern. (d) TEM image of A5-ZnS. (e) and (f) HRTEM images of A5-ZnS. Inset: The corresponding SAED pattern.

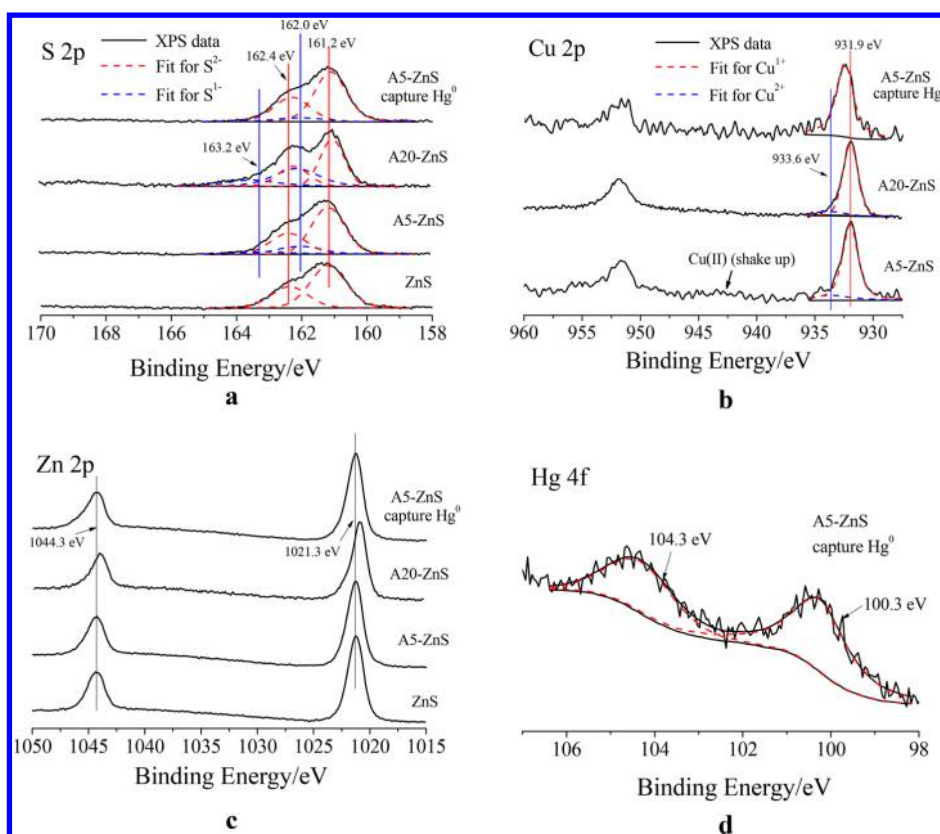


Figure 5. XPS spectra of fresh ZnS, A5-ZnS, A20-ZnS, and A5-ZnS after capture of Hg^0 . (a) S 2p spectra; (b) Cu 2p spectra; (c) Zn 2p spectra; (d) Hg 4f spectrum of A5-ZnS after capture of Hg^0 .

substances were not found in the XRD patterns, even after Cu^{2+} activation for 60 min. The specific area of A60-ZnS was $17.7 \text{ m}^2 \cdot \text{g}^{-1}$, which was similar to that of fresh ZnS. The inset of Figure 4a shows that a positive shift occurred at the diffraction peak corresponding to the (111) crystal facets of ZnS with extension of activation time. The lattice parameters of ZnS, A1-ZnS, A5-ZnS, and A60-ZnS were calculated to be 5.4116, 5.4113, 5.4018, and 5.3912 Å, respectively, suggesting an increasing amount of Cu doped into the ZnS lattice.

TEM and HRTEM were used to study the morphology and crystal structure of ZnS nanoparticles before and after Cu^{2+} activation. Figure 4b shows that the synthesized ZnS presented an irregular spheroid structure with an average diameter of 30–40 nm. The (220) crystal facets of ZnS, with interplanar spacing of 0.19 nm, can be seen clearly in the HRTEM images (Figure 4c). Meanwhile, the clear lattice spot in the selected area electron diffraction (SAED) pattern of ZnS demonstrates the monocrystalline nature of the synthesized ZnS.³³ After activation in $0.005 \text{ mol} \cdot \text{L}^{-1} \text{ Cu}^{2+}$ solution, there were no distinct morphological changes in A5-ZnS and A20-ZnS (Figure 4d and SI Figure S5a). However, as shown in the HRTEM images (Figure 4e,f), the lattice fringes corresponding to (111) crystal facets could be clearly observed in the middle region, but they disappeared at the boundary of the A5-ZnS nanoparticles. Meanwhile, the lattice spot array in the corresponding SAED pattern showed disorder. A similar situation was also observed in the HRTEM images of A20-ZnS (SI Figure S5b,c). The energy-dispersive X-ray spectroscopy (EDX) results show the presence of Cu in A-ZnS nanoparticles (SI Figure S6). Although the obtained Cu contents for A5-ZnS and A20-ZnS were 3.4% and 17.8% (SI

Table S1), respectively, no other lattice fringes associated with copper sulfides were found in the activated region. This indicates that a solid-solution activated interface layer was formed after Cu^{2+} activation. It is difficult to completely replace Zn^{2+} in ZnS with Cu^{2+} due to the size effect, even if the K_{sp} of CuS is far smaller than ZnS.^{34,35} Moreover, the appearance of ZnS changed from white to green after 5 min of activation and then changed to dark green when the activation time was extended to 60 min (shown in SI Figure S4). This also implies that the black CuS and Cu_2S species were not formed during the activation.

3.5. Elemental Composition and Chemical States of the Activated Surface. The XPS spectra of A-ZnS show the presence of Zn, Cu, and S on the surface of the activated layer. The atomic ratios of these were estimated to be 51.7%, 4.0%, and 44.3% for A5-ZnS and 36.0%, 18.5%, and 45.5% for A20-ZnS, respectively (SI Table S2). The atomic ratio of Zn declined with increasing Cu, showing the substitution of Zn by Cu.

As shown in Figure 5, the Zn 2p spectra consisted of two peaks, at ~ 1021.3 and ~ 1044.3 eV, with both peaks being attributed to zinc in Zn–S bonds.³⁶ The $2p_{3/2}$ and $2p_{1/2}$ spin-orbit doublet of the S^{2-} ion is known to be separated by 1.2 eV with an intensity ratio of 2:1.^{23,24} The fitting peaks located at 161.2 and 162.4 eV in the S spectrum of ZnS were consistent with the characteristics of the spin-orbit doublet of the S^{2-} ion (details of the fitting peaks are listed in SI Table S3).^{23,24,37} This indicates that the chemical state of S on the surface of ZnS is assigned only to -2 . However, the doublet of S^{2-} did not fit the S spectrum of A-ZnS. There were additional fitting peaks at 162.0 and 163.2 eV corresponding to the $2p_{3/2}$ and

$2p_{1/2}$ spin-orbit doublet of S^{1-} ,^{23,24,37} suggesting the generation of S^{1-} after activation. Furthermore, the strong fitting peak at 931.9 eV was attributed to Cu^+ because few signals could be observed in the Cu^{2+} shakeup region of the Cu 2p XPS spectra of A-ZnS.³¹ The weak fitting peak located at 933.6 eV in the spectra of A5-ZnS and A20-ZnS was assigned to Cu^{2+} . This results from a small amount of $Cu(OH)_2$ adsorbed on the ZnS surface.^{31,36}

To study further the chemical states of the inner layer, A20-ZnS was bombarded with Ar^+ ions to erode the surface layer by ~ 5 nm. The ratio of Cu decreased from 18.5% to 12.4% after Ar^+ ion denudation. Meanwhile, the XPS spectra (SI Figure S7) show that the chemical state of the doped Cu was Cu^{1+} and that S^{1-} also appeared in the inner layer of ZnS.

3.6. Performance of the Activation Mechanism of Hg^0 Adsorption. The reaction between Cu^{2+} and the ZnS lattice is speculated to be a 1:1 ion exchange of Cu^{2+} for Zn^{2+} , followed by reduction of Cu^{2+} to Cu^{1+} and corresponding oxidation of the S^{2-} ion to S^{1-} . The XPS results show the ratio of S^{1-}/S^{2-} increased from 22.6% to 52.1% with the increase of Cu doped (SI Table S3). S^{1-} is more favorable for stabilizing gaseous Hg^0 than S^{2-} because of its higher oxidation potentials. Therefore, the improvement in the Hg^0 adsorption performance of ZnS can be attributed to the generation of an interface composed of Zn^{2+} , Cu^{1+} , S^{2-} , and S^{1-} after Cu^{2+} activation. After the gaseous Hg^0 was captured, the relative intensity of the S^{1-} fitting peaks of A5-ZnS was obviously weakened (Figure 5) and the atomic ratio of S^{1-}/S^{2-} decreased from 22.6% to 7.7% (SI Table S3). Meanwhile, the $4f_{7/4}$ and $4f_{5/4}$ spin-orbit doublet of Hg^{2+} was observed at 100.3 and 104.3 eV in the Hg 4f XPS spectrum. In addition, the appearance of A5-ZnS changed from green to brown after Hg^0 adsorption, implying the generation of HgS after the capture of Hg^0 . These results prove that S^{1-} on the surface of ZnS was the crucial active site for oxidizing Hg^0 to form stable HgS .

Cu^{2+} activation occurred in two stages. First, Cu^{2+} from the solution was rapidly adsorbed to the ZnS surfaces and then reduced to Cu^{1+} , resulting in the production of S^{1-} on the surface. Owing to the rapid surface activation, the Hg^0 adsorption performance of ZnS was greatly improved after soaking for 1 min. Second, Cu^{2+} gradually diffused through the surface layer to the inner layer, replacing Zn^{2+} in the lattice, where a corresponding redox reaction took place. However, because the adsorption and oxidation of gaseous Hg^0 only occurred on the surface layer of ZnS, the Hg^0 adsorption performance could not be further improved by prolonging the activation time when the surface layers were saturated with Cu^{1+} . As shown in Figure 2b, when the concentration of aqueous Cu^{2+} was <0.005 mol·L⁻¹, the maximum adsorption capacity of A-ZnS increased with increase of Cu^{2+} . This may be attributed to the fact that the proportion of Cu^+ ions doped into the top lattice layer of ZnS increased with increase of the Cu^{2+} in solution, resulting in the generation of a larger proportion of S^{1-} active sites. This enhances the adsorption capacity. However, to maintain the crystal structure of sphalerite, the proportion of Cu doped into the lattice has a limitation. Therefore, the proportion of Cu doped was not enhanced when the concentration of Cu^{2+} increased from 0.005 to 0.01 mol·L⁻¹, and did not cause an obvious change in the maximum adsorption capacity of Hg^0 .

3.7. Hg^0 Recovery and Regeneration of A-ZnS by Cu^{2+} Reactivation. Thermal treatment was used to decompose the chemically adsorbed mercury on the A-ZnS

surface to release the active S species before sorbent regeneration and recovery of the mercury. The temperature-programmed desorption (TPD) curve of A1-ZnS after the first adsorption (Figure 6a) shows that adsorbed mercury was

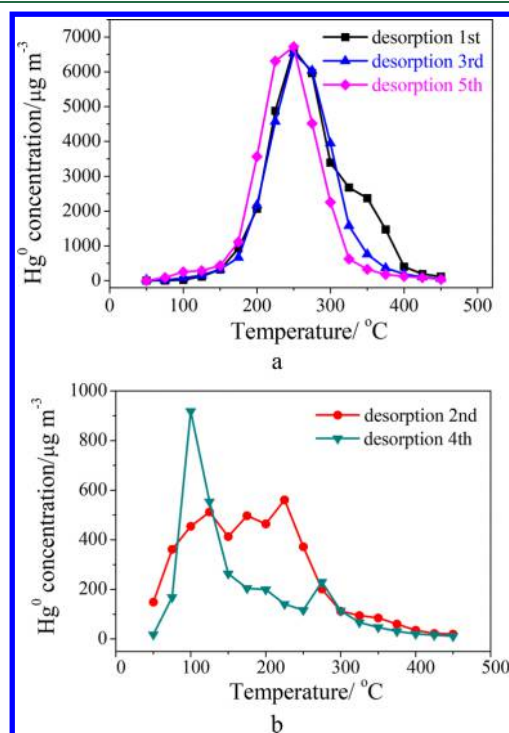


Figure 6. Temperature-programmed desorption curves of Hg^0 after each adsorption in the cyclic experiment of Hg^0 adsorption, Hg^0 recovery, sorbent regeneration. (a) A-ZnS; (b) Nonactivated ZnS.

intensively desorbed in the temperature range of 150–400 °C. The observed desorption peak of Hg^0 at 250 °C corresponds to the decomposition of HgS .^{19,38} The concentration of gaseous Hg^0 in the outlet during this process was enriched to 7 mg·m⁻³. Moreover, this concentration could be further enriched by reducing the N_2 flow, which would facilitate the recovery of gaseous Hg^0 .

To elucidate the role of Cu^{2+} activation in sorbent regeneration, the sorbent was treated with H_2O instead of a Cu^{2+} solution before the second and fourth adsorptions. As shown in Figure 7, the Hg^0 adsorption breakthrough curves of the first, third, and fifth adsorption tests, in which the sorbent had been activated by Cu^{2+} , exhibited similar trends. However, an obvious reduction in Hg^0 adsorption activity was observed during the second and fourth adsorptions. The corresponding TPD profile (Figure 6b) shows that a large amount of Hg^0 was released below 150 °C, and that a desorption peak appeared at 100 °C, indicating that most of the Hg^0 was physically adsorbed to ZnS. This suggests that the S^{1-} active site on the surface of ZnS disappeared and could not be recovered by thermal treatment, even if mercury species adsorbed to the surface had been released. By comparison, because of the activation with Cu^{2+} before the third and fifth adsorptions, the Hg^0 adsorption performance recovered to the original level. Meanwhile, the corresponding TPD profile shows that the desorption peak of Hg^0 returned to 250 °C, and that few gaseous Hg^0 atoms were observed below 150 °C. These results suggest that a new activated interface was regenerated on the

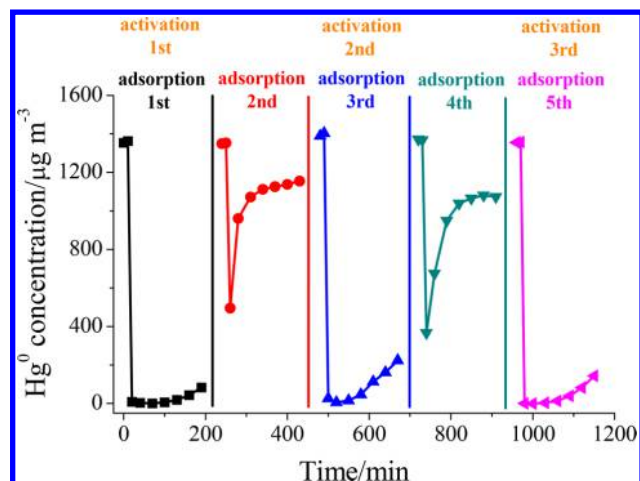


Figure 7. Hg^0 adsorption breakthrough curves of Al-ZnS during five cycles of Hg^0 adsorption, Hg^0 recovery, and sorbent regeneration. Reaction conditions: sorbent mass = 50 mg, total flow rate = 500 mL min^{-1} , adsorption temperature = 60 °C, adsorption time = 3 h, and $[\text{Hg}^0] = 1.3\text{--}1.4 \text{ mg}\cdot\text{m}^{-3}$.

surface, resulting in the oxidation of the physically adsorbed Hg^0 to form stable HgS .

Another cyclic experiment is shown in SI Figure S8, in which the activation time was prolonged to 60 min to ensure full activation of the surface of ZnS before each adsorption test. The results show that the Hg^0 adsorption capacity was maintained at $\sim 60 \mu\text{g}$ during the five cycles. They further demonstrate that the activated surface can be recovered by Cu activation after thermal treatment, thus maintaining good performance for Hg^0 adsorption.

Not only is Cu^{2+} activation an effective interface modification method for enhancing Hg^0 adsorption capacity, and restoring the sorbent performance of ZnS and natural sphalerite, but these results may extend to other chalcogenide sorbents as well. A small amount of Cu^{2+} ions can activate the surface layer of ZnS to develop functional mercury-enrichment sorbents, and sphalerite is abundant in nature. Thus, this Cu^{2+} activation method could make zinc-ore concentrate a promising sorbent at great cost advantage for removing mercury pollutants from smelting flue gas.

■ ASSOCIATED CONTENT

📄 Supporting Information

The Supporting Information is available free of charge on the ACS Publications website at DOI: 10.1021/acs.est.9b01310.

Elemental composition as determined by XPS and EDX. Details of XPS fitting. A sketch of the Hg^0 adsorption evaluation system. Hg^0 adsorption breakthrough curves of A-ZnS. Photographs of the appearances of sorbents. TEM and HRTEM of A20-ZnS. EDX spectra of A-ZnS. XPS spectra of A20-ZnS after denudation. The Hg^0 adsorption capacity of A60-ZnS in five cyclic tests (PDF)

■ AUTHOR INFORMATION

Corresponding Author

*Phone: 86-021-54745591; e-mail: quzan@sytu.edu.cn.

ORCID

Zan Qu: 0000-0003-3736-4548

Notes

The authors declare no competing financial interest.

■ ACKNOWLEDGMENTS

This study was supported by the National Key R&D Program of China (2017YFC0210500 and 2017YFC0806300) and by the National Natural Science Foundation of China (No. 51478261 and 21806105).

■ REFERENCES

- (1) Boening, D. W. Ecological effects, transport, and fate of mercury: A general review. *Chemosphere* **2000**, *40* (12), 1335–1351.
- (2) Wang, S. X.; Liu, M.; Jiang, J. K.; Hao, J. M.; Ye, W. U.; Gstreets, D. Estimate the mercury emissions from non-coal sources in China. *China Environmental Science* **2006**, *12*.
- (3) Zhang, L.; Wang, S. X.; Long, W.; Ye, W.; Duan, L.; Wu, Q. R.; Mei, Y.; Hai, Y.; Hao, J. M. Updated emission inventories for speciated atmospheric mercury from anthropogenic sources in China. *Environ. Sci. Technol.* **2015**, *49* (5), 3185.
- (4) Huang, Y.; Deng, M.; Li, T.; Japenga, J.; Chen, Q.; Yang, X. Anthropogenic mercury emissions from 1980 to 2012 in China. *Environ. Pollut.* **2017**, 226.230
- (5) Lin, Y.; Wang, S.; Steindal, E. H.; Wang, Z.; Braaten, H. F. V.; Wu, Q.; Larssen, T. A holistic perspective is needed to ensure success of Minamata Convention on Mercury. *Environ. Sci. Technol.* **2017**, *51* (3), 1070–1071.
- (6) Wu, Q. R.; Wang, S. X.; Zhang, L.; Song, J. X. Update of mercury emissions from China's primary zinc, lead and copper smelters, 2000–2010. *Atmos. Chem. Phys.* **2012**, *12* (22), 11153–11163.
- (7) Pacyna, E. G.; Pacyna, J. M. Global emission of mercury from anthropogenic sources in 1995. *Water, Air, Soil Pollut.* **2002**, *137* (1–4), 149–165.
- (8) Gao, Y. S.; Zhang, Z.; Wu, J. W.; Duan, L. H.; Umar, A.; Sun, L. Y.; Guo, Z. H.; Wang, Q. A critical review on the heterogeneous catalytic oxidation of elemental mercury in flue gases. *Environ. Sci. Technol.* **2013**, *47* (19), 10813–10823.
- (9) Wang, S. X.; Song, J. X.; Li, G. H.; Wu, Y.; Zhang, L.; Wan, Q.; Streets, D. G.; Chin, C. K.; Hao, J. M. Estimating mercury emissions from a zinc smelter in relation to China's mercury control policies. *Environ. Pollut.* **2010**, *158* (10), 3347–3353.
- (10) Pavlish, J. H.; Sondreal, E. A.; Mann, M. D.; Olson, E. S.; Galbreath, K. C.; Laudal, D. L.; Benson, S. A. Status review of mercury control options for coal-fired power plants. *Fuel Process. Technol.* **2003**, *82* (2–3), 89–165.
- (11) Hylander, L. D.; Herbert, R. B. Global emission and production of mercury during the pyrometallurgical extraction of nonferrous sulfide ores. *Environ. Sci. Technol.* **2008**, *42* (16), 5971–5977.
- (12) Allgulin, T. Method for eliminating traces of mercury in gases. EP1316353-A3.
- (13) Ma, Y.; Xu, H.; Qu, Z.; Yan, N.; Wang, W. Absorption characteristics of elemental mercury in mercury chloride solutions. *J. Environ. Sci.* **2014**, *26* (11), 2257–2265.
- (14) Ma, Y. P.; Qu, Z.; Xu, H. M.; Wang, W. H.; Yan, N. Q. Investigation on mercury removal method from flue gas in the presence of sulfur dioxide. *J. Hazard. Mater.* **2014**, *279*, 289–295.
- (15) Liu, Y.; Wang, Q. F.; Mei, R. J.; Wang, H. Q.; Weng, X. L.; Wu, Z. B. Mercury re-emission in flue gas multipollutants simultaneous absorption system. *Environ. Sci. Technol.* **2014**, *48* (23), 14025–14030.
- (16) Guo, Y.; Li, Y.; Wang, J.; Zhu, T.; Ye, M. Effects of activated carbon properties on chlorobenzene adsorption and adsorption product analysis. *Chem. Eng. J.* **2014**, *236* (1), 506–512.
- (17) Ma, Y. P.; Mu, B. L.; Zhang, X. J.; Yuan, D. L.; M, C.; Xu, H. M.; Qu, Z.; Fang, S. M. Graphene enhanced Mn-Ce binary metal oxides for catalytic oxidation and adsorption of elemental mercury from coal-fired flue gas. *Chem. Eng. J.* **2019**, *358*, 1499–1506.
- (18) Liao, Y.; Xiong, S.; Dang, H.; Xiao, X.; Yang, S.; Wong, P. K. The centralized control of elemental mercury emission from the flue

gas by a magnetic regenerable Fe-Ti-Mn spinel. *J. Hazard. Mater.* **2015**, *299*, 740–6.

(19) Liao, Y.; Chen, D.; Zou, S.; Xiong, S.; Xiao, X.; Dang, H.; Chen, T.; Yang, S. Recyclable naturally derived magnetic pyrrhotite for elemental mercury recovery from flue gas. *Environ. Sci. Technol.* **2016**, *50* (19), 10562–10569.

(20) Lin, Y.; Cook, N. J.; Ciobanu, C. L.; Liu, Y.; Zhang, Q.; Liu, T.; Gao, W.; Yang, Y.; Danyushevskiy, L. Trace and minor elements in sphalerite from base metal deposits in South China: A LA-ICPMS study. *Ore Geol. Rev.* **2011**, *39* (4), 188–217.

(21) Li, H.; Zhu, L.; Wang, J.; Li, L.; Shih, K. Development of nano-sulfide sorbent for efficient removal of elemental mercury from coal combustion fuel gas. *Environ. Sci. Technol.* **2016**, *50* (17), 9551–9557.

(22) Xu, H.; Yuan, Y.; Liao, Y.; Xie, J.; Qu, Z.; Shangguan, W.; Yan, N. $[\text{MoS}_4]^{2-}$ cluster bridges in Co–Fe layered double hydroxides for mercury uptake from S–Hg mixed flue gas. *Environ. Sci. Technol.* **2017**, *51* (17), 10109–10116.

(23) Kartio, I. J. An XPS study of sphalerite activation by copper. *Langmuir* **1998**, *14* (18), 5274–5278.

(24) Smart, R. S. C. XPS of sulphide mineral surfaces metal-deficient, polysulphides, defects and elemental sulphur. *Surf. Interface Anal.* **1999**, *28*, 101–105.

(25) Liu, J.; Wen, S.; Deng, J.; Chen, X.; Feng, Q. DFT study of ethyl xanthate interaction with sphalerite (110) surface in the absence and presence of copper. *Appl. Surf. Sci.* **2014**, *311*, 258–263.

(26) Chandra, A. P.; Gerson, A. R. A review of the fundamental studies of the copper activation mechanisms for selective flotation of the sulfide minerals, sphalerite and pyrite. *Adv. Colloid Interface Sci.* **2009**, *145* (1–2), 97–110.

(27) Hao, X.; Wang, Y.; Zhou, J.; Cui, Z.; Wang, Y.; Zou, Z. Zinc vacancy-promoted photocatalytic activity and photostability of ZnS for efficient visible-light-driven hydrogen evolution. *Appl. Catal., B* **2018**, *221*, 302–311.

(28) Liao, Y.; Xia, Y.; Zou, S.; Liu, P.; Liang, X.; Yang, S. In situ emergency disposal of liquid mercury leakage by Fe-containing sphalerite: Performance and reaction mechanism. *Ind. Eng. Chem. Res.* **2017**, *56* (1), 153–160.

(29) Yang, S. J.; Guo, Y. F.; Yan, N. Q.; Qu, Z.; Xie, J. K.; Yang, C.; Jia, J. P. Capture of gaseous elemental mercury from flue gas using a magnetic and sulfur poisoning resistant sorbent Mn/gamma-Fe₂O₃ at lower temperatures. *J. Hazard. Mater.* **2011**, *186* (1), 508–515.

(30) Xu, H.; Yan, N.; Qu, Z.; Liu, W.; Mei, J.; Huang, W.; Zhao, S. Gaseous heterogeneous catalytic reactions over Mn-Based oxides for environmental applications: A critical review. *Environ. Sci. Technol.* **2017**, *51* (16), 8879–8892.

(31) Liu, J.; Wen, S.; Wang, Y.; Deng, J.; Chen, X. Transition state search study on the migration of Cu absorbed on the S sites of sphalerite (110) surface. *Int. J. Miner. Process.* **2016**, *147*, 28–30.

(32) Buckley, A. N.; Skinner, W. M.; Harmer, S. L.; Pring, A.; Lamb, R. N.; Fan, L.-J.; Yang, Y.-w. Examination of the proposition that Cu(II) can be required for charge neutrality in a sulfide lattice - Cu in tetrahedrites and sphalerite. *Can. J. Chem.* **2007**, *85* (10), 767–781.

(33) Nong, S.; Dong, W.; Yin, J.; Dong, B.; Lu, Y.; Yuan, X.; Wang, X.; Bu, K.; Chen, M.; Jiang, S.; Liu, L. M.; Sui, M.; Huang, F. Well-dispersed ruthenium in mesoporous crystal TiO₂ as an advanced electrocatalyst for hydrogen evolution reaction. *J. Am. Chem. Soc.* **2018**, *140* (17), 5719–5727.

(34) Qu, Z.; Yan, L.; Li, L.; Xu, J.; Liu, M.; Li, Z.; Yan, N. Ultraeffective ZnS nanocrystals sorbent for mercury(II) removal based on size-dependent cation exchange. *ACS Appl. Mater. Interfaces* **2014**, *6* (20), 18026–32.

(35) Xu, J.; Qu, Z.; Yan, N.; Zhao, Y.; Xu, X.; Liang, L. Size-dependent nanocrystal sorbent for copper removal from water. *Chem. Eng. J.* **2016**, *284*, 565–570.

(36) Harmer, S. L. The effect of bulk iron concentration and heterogeneities on the copper activation of sphalerite. *Miner. Eng.* **2008**, *21*, 1005–1021.

(37) Ghahremaninezhad, A.; Dixon, D. G.; Asselin, E. Electrochemical and XPS analysis of chalcopyrite (CuFeS₂) dissolution in sulfuric acid solution. *Electrochim. Acta* **2013**, *87*, 97–112.

(38) Zhao, H. T.; Yang, G.; Gao, X.; Pang, C. H.; Kingman, S. W.; Wu, T. Hg⁰ capture over CoMoS/gamma-Al₂O₃ with MoS₂ nanosheets at low temperatures. *Environ. Sci. Technol.* **2016**, *50* (2), 1056–1064.